ACS APPLIED MATERIALS & INTERFACES

Research Article

Cite This: ACS Appl. Mater. Interfaces 2018, 10, 28789−28795

www.acsami.org

Topological Insulator GMR Straintronics for Low-Power Strain Sensors

Lingzhi Li,[†,∥] Yunhua Wang,[*,‡,§,∥] Zongtan Wang,[†] Yulan Liu,[†] and Biao Wang[*,‡,§]

[†]School of Engineering, Sun Yat-sen University, Guangzhou 510006, China

[‡]Sino-French Institute of Nuclear Engineering and Technology, Sun Yat-sen University, Zhuhai 519082, China

[§]State Key Laboratory of Optoelectronic Materials and Technologies, Sun Yat-sen University, Guangzhou 510275, China

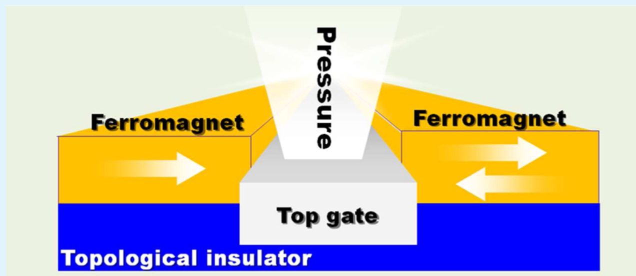

ABSTRACT: A quantum spin Hall insulator, i.e., topological insulator (TI), is a natural candidate for low-power electronics and spintronics because of its intrinsic dissipationless feature. Recent density functional theory and scanning tunneling spectroscopy experiments show that the mechanical strain allows dynamic, continuous, and reversible modulations of the topological surface states within the topological phase and hence opens prospects for TI straintronics. Here, we combine the mechanical strain and the giant magnetoresistance (GMR) of a ferromagnet−TI (FM−TI) junction to construct a novel TI GMR straintronics device. Such a FM−strained-FM−TI junction permits several energy spectral ranges for 100% GMR and a robust strain-controllable magnetic switch. Beyond the 100% GMR energy range, we observe a strain-modulated oscillating GMR, which is an alternative hallmark of the Fabry-Pérot quantum interference of Dirac surface states. These strain-sensitive GMR responses indicate that FM−strained-FM−TI junctions are very favorable for practical applications for low-power nanoscale strain sensors.

KEYWORDS: *topological insulator, giant magnetoresistance, magnetic switch, strain sensor, Fabry-Pérot quantum resonances*

1. INTRODUCTION

A three-dimensional (3D) topological insulator (TI) belongs to a new quantum state of matter characterized by the nontrivial Z_2-order parameter with an insulating bulk state and the protected metallic surface states.[1−5] One of the most exotic features for TI is that the combination of strong spin−orbit coupling and time-reversal symmetry allows the spin-momentum locked helical surface Dirac fermions, which are responsible for many exotic physical properties of TI. The striking second generation of TI, including Bi_2Se_3, Bi_2Te_3, and Sb_2Te_3, provides an ideal platform for the research of fundamental topological phenomena at room temperature[6−9] because of its high purity and simple surface band structure, i.e., large bulk band gap and single Dirac cone, which are confirmed by angle-resolved photoemission spectroscopy and scanning tunneling microscopy.

The interaction between magnetism and surface states of TI has attracted considerable attention for the fundamental interests including the topological magnetoelectric effect,[10−12] quantized anomalous Hall effect,[13−15] massive Dirac fermion,[16] geometrical phase,[17] and chiral edge currents,[18] where the ferromagnetism is spontaneous in a magnetically doped TI. In addition, experiments demonstrate that the external magnetic proximity effect can also enable a remarkable ferromagnetic exchange field on the surface of TI at ambient temperature.[19,20] In this regard, both the ballistic and diffusive magnetotransports (especially, tunneling and giant magnetoresistance (GMR) effects) in various ferromagnet (FM)/TI junctions have been highly investigated,[21−37] for the potential applications in information processing and storage. Recent works on the controllability of magnetoresistance through a FM/TI junction concern gate voltage,[21−27] magnetization direction,[28−30] superlattice effects,[31] magnetic field magnitude,[32] domain-wall modulation,[33] and impurity scatterings.[34]

A mechanical strain can induce the topological phase transition between a common insulator or semimetal and TI (e.g., Bi_2Se_3,[38,39] Sb_2Se_3,[39−41] InSb,[42] Li_2IrO_3,[43] $TiTe_2$,[44] BiTeI,[45−47] trigonal tellurium,[48] HgTe,[49] HgSe,[50] KNa_2Bi,[51] NaBaBi,[52] and Na_3Bi).[53] Therefore, a strain offers an alternative way to realize TI. A strain can also tune the surface electronic structure and electronic transports of both 3D TI and topological crystalline insulator (TCI) with keeping the topological phases.[38,39,54−63] For 3D TCI, the lattice mismatch induces strain, which shifts the Dirac points in the surface Brillouin zone like an effective magnetic vector potential.[59,60] For 3D TI, a typical hydrostatic pressure allows a uniaxial compressive strain, which makes a monotonic downshift of the Dirac points with respect to energy like a negative electrostatic potential.[38,39,55−57] Compared with doping, the mechanical strain permits dynamic, continuous, and reversible modulations. Therefore, strain modulation is favorable for practical applications. Herein, we report the GMR response to strain in

Received: June 10, 2018
Accepted: July 30, 2018
Published: July 30, 2018

DOI: 10.1021/acsami.8b09664
ACS Appl. Mater. Interfaces 2018, 10, 28789−28795

a FM−strained-FM−TI junction (see Figure 1). On the basis of the energy spectrum analysis of propagating states, we obtain several types of energy spectral ranges for 100% GMR. By virtue of the magnetotransport calculations, we find a strain-controllable magnetic switch effect with a conversion between an insulating state with no GMR signal and a conducting state with 100% GMR response. We also find that a strain-modulated Fabry-Pérot resonance renders a remarkable oscillating GMR effect in the FM−TI nanostructure. These results show that the TI GMR straintronics is suitable for low-power nanoscale strain sensors.

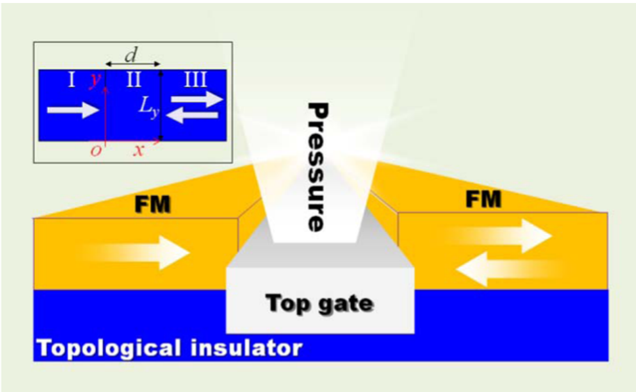

Figure 1. Setup for topological insulator GMR straintronics. The device consists of a FM−strained-FM junction on the top surface of 3D TI (layered Bi_2Se_3). In the left (I) and right (III) FM regions, the longitudinal magnetizations can be parallel (P) or antiparallel (AP) to the applied x-directional bias for GMR. In the middle (II) region with width d, the top gate supplies a voltage U_g and transfers a uniform hydrostatic pressure to the TI. The inset shows the top view of the top $x-y$ surface of TI.

2. THEORY

We consider a FM−strained-FM junction on the top surface of a 3D TI (layered Bi_2Se_3), as shown in Figure 1, where a bias is applied in the x direction, a top gate in the middle region (II) with the width d supplies a voltage U_g and transfers a uniform hydrostatic pressure to the TI, and the planar magnetizations denoted by the white arrows in the left region (I) and right region (III) are parallel (P) or antiparallel (AP) to the applied bias. In this work, we focus on the magnetotransport response to the longitudinal ferromagnetic exchange field.[35] To capture the main physical picture, it is usually assumed that the proximity-effect-induced ferromagnetism region has a step boundary.[22−24,26−29,37] Therefore, we write the ferromagnetic exchange field profile as $\vec{M}(x) = M_x[\Theta(-x) + \eta\Theta(x-d)]\vec{e}_x$, where $\Theta(x)$ is the Heaviside step function and η is 1 and −1 for P and AP configurations, respectively. Similarly, the potential profile of the junction is approximately expressed by $V(x) = (U_g - U_s)\Theta(x)\Theta(d-x)$, with the gate voltage (U_g) and the strain-induced negative potential ($-U_s$). In this regard, the effective low-energy Hamiltonian of the surface states for the system under consideration reads

$$\hat{H} = v_F(\vec{\sigma}\times\vec{k})\cdot\vec{e}_z + \vec{\sigma}\cdot\vec{M}(x) + V(x)\sigma_0 \quad (1)$$

where $v_F = 4.08$ eV Å is the Fermi velocity of the surface states for Bi_2Se_3, $\vec{\sigma}$ is the vector of Pauli spin matrices, $\vec{k}$ is the electron momentum, and σ_0 is the 2 × 2 identity matrix. Considering the y-direction momentum conservation, we write the wave functions in the region j (j = I, II, and III) along the $\pm x$ directions as $\psi_j^\pm(x,y) = \psi_j^\pm(x)e^{ik_y y}$, where $\psi_j^\pm(x)$ is obtained from eq 1 and takes the form as

$$\psi_j^\pm(x) = e^{\pm ik_{x,j}x}\begin{pmatrix} 1 \\ \dfrac{v_F k_{y,j} \mp iv_F k_{x,j}}{E - V(x)} \end{pmatrix} \quad (2)$$

For the three regions, we have $k_{y,I} = M_x/v_F + k_y$, $k_{x,I} = \mathrm{sgn}(E)(E^2/v_F^2 - k_{y,I}^2)^{1/2}$, $k_{x,II} = \mathrm{sgn}(E - V)((E - V)^2/v_F^2 - k_y^2)^{1/2}$, $k_{y,II} = k_y$, $k_{x,III} = \mathrm{sgn}(E)(E^2/v_F^2 - k_{y,III}^2)^{1/2}$, and $k_{y,III} = \eta M_x/v_F + k_y$. The incident angle is defined by $\theta = \arcsin(v_F k_{y,I}/E)$, and the group velocities in the three regions take the forms as $v_{x,I} = v_F^2 k_{x,I}/E$, $v_{x,II} = v_F^2 k_{x,II}/(E - V)$, and $v_{x,III} = v_F^2 k_{x,III}/E$, respectively. To guarantee the current conservation with a normalized incident probability density, we write the total wave functions in the three regions as

$$\begin{cases} \psi_I(x) = (\psi_I^+(x) + r\psi_I^-(x))/\sqrt{2|v_{x,I}|} \\ \psi_{II}(x) = (a\psi_{II}^+(x) + b\psi_{II}^-(x))/\sqrt{2|v_{x,II}|} \\ \psi_{III}(x) = t\psi_I^+(x)/\sqrt{2|v_{x,III}|} \end{cases} \quad (3)$$

where r is the reflection coefficient, t is the transmission coefficient, and a and b are the unknown complex coefficients. Using the continuity of two-component wave functions in real spin space at the left ($x = 0$) and right ($x = d$) boundaries, we can obtain the corresponding transmission probability for P (η = 1) and AP ($\eta = -1$) configurations, as follows

$$T_\eta(E, V, M_x, k_y) = \frac{k_{x,III}}{k_{x,I}} \left| \frac{(\alpha - \alpha^*)(\beta - \beta^*)}{e^{ik_{x,II}d}(\beta^* - \alpha^*)(\beta - \gamma_\eta) - e^{-ik_{x,II}d}(\beta - \alpha^*)(\beta^* - \gamma_\eta)} \right|^2 \quad (4)$$

where the upper index asterisk denotes the complex conjugate, $\alpha = (v_F k_{y,I} - iv_F k_{x,I})/E$, $\beta = (v_F k_y - iv_F k_{x,II})/(E - V)$, and $\gamma_\eta = (\eta M_x + v_F k_y - iv_F k_{x,III})/E$. We focus on the ballistic transport system with few impurities. For this case, the conductance for a small bias at finite temperature reads

$$G_\eta(E, V, M_x) = G_0 \int dE \int T_\eta(E, V, M_x, k_y)\frac{-\partial f}{\partial E}dk_y \quad (5)$$

where $G_0 = e^2L_y/\pi h$ is the conductance unit with the y-direction width L_y = 400 nm and $f(E) = 1/(e^{(E-E_F)/k_BT} + 1)$ is the Fermi−Dirac distribution function. If a very low temperature is considered, the above formula is further written as

$$G_\eta(E_F, V, M_x) = G_0 \int T_\eta(E_F, V, M_x, k_y)\, dk_y \quad (6)$$

Then, the GMR is defined as

$$\mathrm{GMR} = (1 - G_{AP}/G_P) \times 100\% \quad (7)$$

3. RESULTS AND DISCUSSION

3.1. Energy Spectral Range for Strain-Dependent 100% GMR. Before we discuss the strain-dependent energy spectra, let us comment on the strain effects on the Dirac

DOI: 10.1021/acsami.8b09664
ACS Appl. Mater. Interfaces 2018, 10, 28789−28795

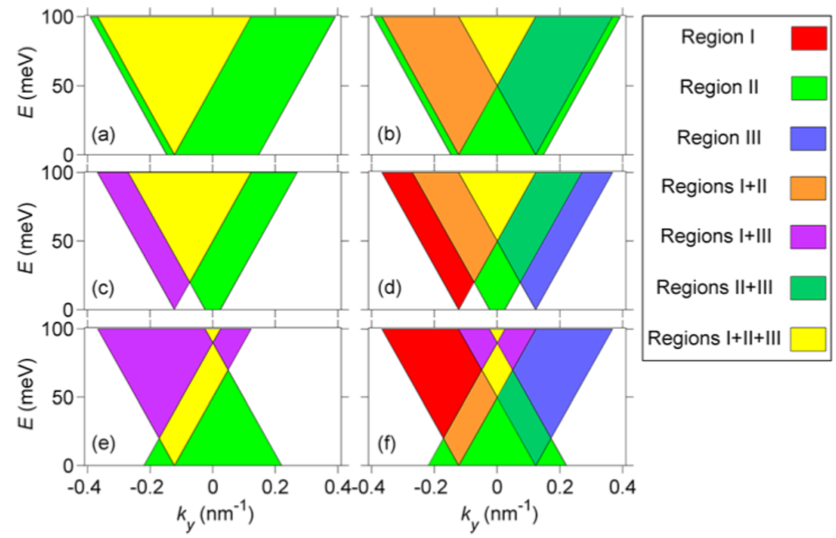

Figure 2. Energy spectra of propagating states through the FM−strained-FM−TI junction in the (k_y, E) space. Type A with M_x = 50 meV, U_s = 60 meV, and U_g = 0 meV for (a) P and (b) AP configurations. Type B with M_x = 50 meV, U_s = 10 meV, and U_g = 0 meV for (c) P and (d) AP configurations. Type C with M_x = 50 meV, U_s = 10 meV, and U_g = 100 meV for (e) P and (f) AP configurations. The overlapped yellow areas by the energy spectra of all of the three regions, i.e., I + II + III, allow the propagating waves across the entire junction.

Table 1. Three Types of GMR Energy Spectral Range for the FM−Strained-FM−TI Junction

type	V vs M_x	range of E for 100% GMR	range of k_y for 100% GMR
A	$V < -M_x$	$0 \leq E \leq M_x$	$-2M_x \leq v_F k_y \leq 0$
B	$-M_x \leq V \leq M_x$	$(V + M_x)/2 \leq E \leq M_x$	$V - M_x \leq v_F k_y \leq 0$
C	$V > M_x$	$0 \leq E \leq M_x$	$-(V + M_x)/2 \leq v_F k_y \leq 0$

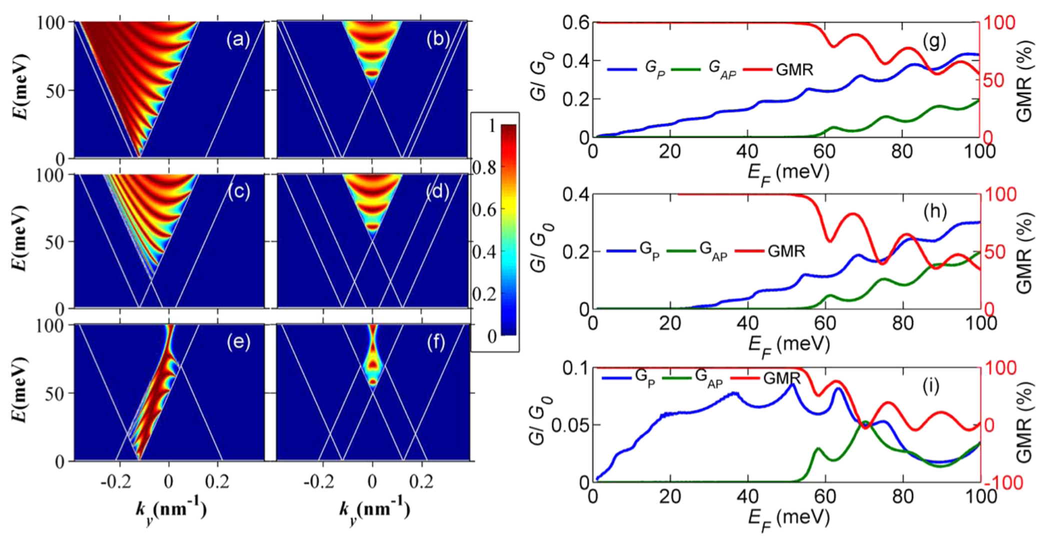

Figure 3. Contour plots of transmission probability through the FM−strained-FM−TI junction as a function of k_y and E for (a) P and (b) AP configurations of type A, (c) P and (d) AP configurations of type B, and (e) P and (f) AP configurations of type C, with the same corresponding parameters as in Figure 2. Conductance G_P and G_{AP} and GMR as a function of energy E_F for (g) type A, (h) type B, and (i) type C. For all cases, d = 100 nm.

surface states of Bi_2Se_3. According to the first-principles calculations,[38,55,56] it can be summarized that the topological insulating phase for layered Bi_2Se_3 remains if the strain is less than 6.4%[38] and that the negative electrostatic potential $(-U_s)$ induced by the compressive uniaxial strain can be roughly approximated as two linear piecewise functions of strain: For $0 < \varepsilon \leq 3\%$, $U_s = 2\varepsilon$, and for $3\% < \varepsilon \leq 6.4\%$, $U_s = 3.5\varepsilon - 0.045$, in units of eV.[55] If a compressive strain larger than 6.4% is applied, the bulk gap will be closed, and the phase transition for layered Bi_2Se_3 from TI to a common insulator happens. Consequently, the Dirac bands are broken by the large strain.[56] Therefore, in this work, the applied strain is limited to 6.4% and U_s is correspondingly less than 0.179 eV.

Now we begin to perform energy spectrum analysis. The definition of GMR in eq 7 shows that the positive 100% GMR occurs if there exists an energy spectral range with $G_{AP} = 0$ and $G_P \neq 0$. In general, both the propagating and nonpropagating (evanescent) states in middle region II contribute to the

DOI: 10.1021/acsami.8b09664
ACS Appl. Mater. Interfaces 2018, 10, 28789−28795

conductance. However, the tunneling of evanescent surface Dirac states in region II rapidly vanishes with the increase of the width d, as demonstrated in eq 4. Thus, if a relatively large width d is adopted in region II, the contribution to conductance by evanescent mode is well negligible. Then, we can approximately use the energy spectra of propagating states to determine the energy range of 100% GMR. Figure 2 shows the energy spectra of propagating states in the (k_y, E) space for both P and AP configurations of the FM−strained-FM−TI junction. As we can see, in the (k_y, E) space, the in-plane magnetic exchange field M_x shifts the original Dirac point (0, 0) to the new position $(-M_x/v_F, 0)$ in magnetic regions I and III for P configuration, but for AP configuration, the exchange field shifts the original Dirac point (0, 0) to $(M_x/v_F, 0)$ in region III. The total potential V involving the gate voltage U_g and the compressive-strain-induced negative potential $(-U_s)$ moves down or up the Dirac cone in middle region II. Therefore, to determine the GMR energy spectral range, we should further make clear the interplay among M_x, U_g, and U_s. By comparing the sizes between V and M_x and taking the range of k_y into account, we classify the GMR energy spectral range into three types, as demonstrated in Table 1.

For type A in Figure 2a,b, $V < -M_x$, $G_P \neq 0$ for the positive energy, $G_{AP} = 0$ for $0 \leq E \leq M_x$ and hence the energy range for the 100% GMR is from 0 to M_x. For type B, as shown in Figure 2c,d, $-M_x \leq V \leq M_x$, $G_P = 0$ for $0 \leq E \leq (V + M_x)/2$, $G_{AP} = 0$ for $0 \leq E \leq M_x$, and $G_P \neq 0$ for $E > (V + M_x)/2$. Therefore, the energy range of the 100% GMR for type B is from $(V + M_x)/2$ to M_x. For type C in Figure 2e,f, $V > M_x$, $G_P \neq 0$ for the positive energy, $G_{AP} = 0$ for $0 \leq E \leq M_x$ and hence the energy range for the perfect GMR is from 0 to M_x. We note that there exists a forbidden energy range for both P and AP configurations in type B and the energy ranges for the 100% GMR in both types A and C are consistent, but the ranges of k_y are different, as demonstrated in Table 1.

To demonstrate the 100% GMR energy range determined by the energy spectrum analysis of propagating states and the features of the three types, we further numerically calculate the transmission (Figure 3a−f), conductance, and GMR (Figure 3g−i), where the width d is taken as 100 nm such that the contribution of conductance is almost entirely attributed to the propagating states. As predicted above, the transmission energy and angle ranges of the propagating states, the zero and nonzero conductance areas, and the 100% GMR energy range agree well with the energy spectrum analysis. Beyond the perfect GMR energy range, the oscillating GMR related to the transmission resonance occurs, and it will be studied later. Since the three types depend on the relation among M_x, U_g, and U_s, the three types with the 100% GMR can be tuned by strain if U_g and M_x are fixed. Although the compressive strain acts as a negative potential, the strain-sensing effect rather than a negative voltage is necessary for a TI strain sensor. For type B, we also indeed observe a forbidden energy range for both P and AP configurations, where the GMR does not exist. The cutoff value between the forbidden and 100% GMR energy ranges is determined by $(U_g - U_s + M_x)/2$. Such a sharp strain-modulated GMR response from no GMR signal to 100% GMR is very suitable for strain (pressure) sensors and strain-controllable magnetic switches.

3.2. Strain-Controllable Magnetic Switch. As figured out above, for type B, the applied strain can change the zero-conductance cutoff value for the P configuration, but the zero-conductance cutoff value for the AP case is unchangeable by strain, as shown in Figure 3h. This property motivates us to construct a novel strain-controllable magnetic switch. To illustrate the features of the magnetic switch, we define two states: the insulating state with no GMR (ISNG) and the switched state with perfect GMR (SSPG). The conductance as a function of strain is presented in Figure 4, where the light green and yellow backgrounds denote the strain ranges for ISNG and SSPG, respectively. Using the cutoff value $E = (U_g - U_s + M_x)/2$ for type B, we obtain the cutoff strain from ISNG to SSPG

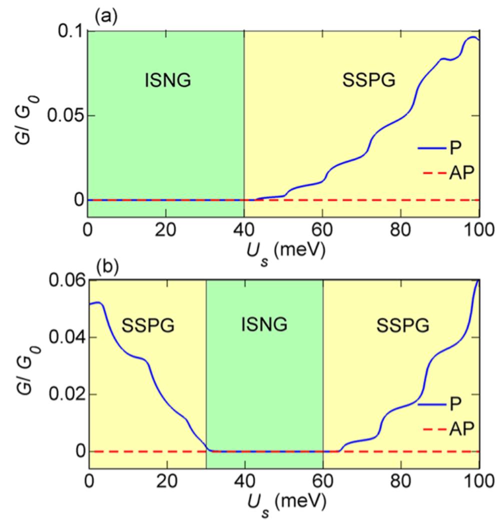

Figure 4. Conductance G_P and G_{AP} as a function of strain-induced potential U_s. (a) M_x = 50 meV, U_g = 40 meV; (b) M_x = 40 meV, U_g = 70 meV. For all cases, E_F = 25 meV and d = 100 nm. The state ISNG is represented by the light green areas, and the state SSPG is represented by the light yellow areas. The strain-controllable magnetic switch has a single cutoff value in (a) for the conversion ISNG → SSPG and double strain cutoff values in (b) for the conversion SSPG → ISNG → SSPG.

$$U_s(\text{ISNG} \rightarrow \text{SSPG}) = U_g + M_x - 2E \tag{8}$$

From Figure 4a, we can observe the magnetic switch with only single strain cutoff value U_s(ISNG → SSPG) and its converting route ISNG → SSPG with increasing the strain. If a larger U_g is given by the top gate with $U_g > M_x$, the GMR energy range belongs to type C for a small strain. However, with the enhanced strain, the GMR energy range is changed from type C to B. Therefore, one can also realize a magnetic switch with double strain cutoff values. The other cutoff value is given by

$$U_s(\text{SSPG} \rightarrow \text{ISNG}) = U_g - M_x \tag{9}$$

From Figure 4b, we can see the strain-controllable GMR switch with double cutoff values and its converting route SSPG → ISNG → SSPG. In an actual system, thermal fluctuations and contact resistance may slightly reduce the switch effect.[54] However, the large energy intervals and accessible value of G_P make the strain-manipulated magnetic switch practical in experiments.

3.3. Strain-Modulated Fabry-Pérot Resonance and Oscillating GMR. Because of the Dirac linear dispersion for the surface states, the unique Fabry-Pérot quantum interference of the surface states has attracted considerable attention in both fundamental interest and practical applications in TI.[64−69] For the considered FM−strained-FM−TI junction,

DOI: 10.1021/acsami.8b09664
ACS Appl. Mater. Interfaces 2018, 10, 28789−28795

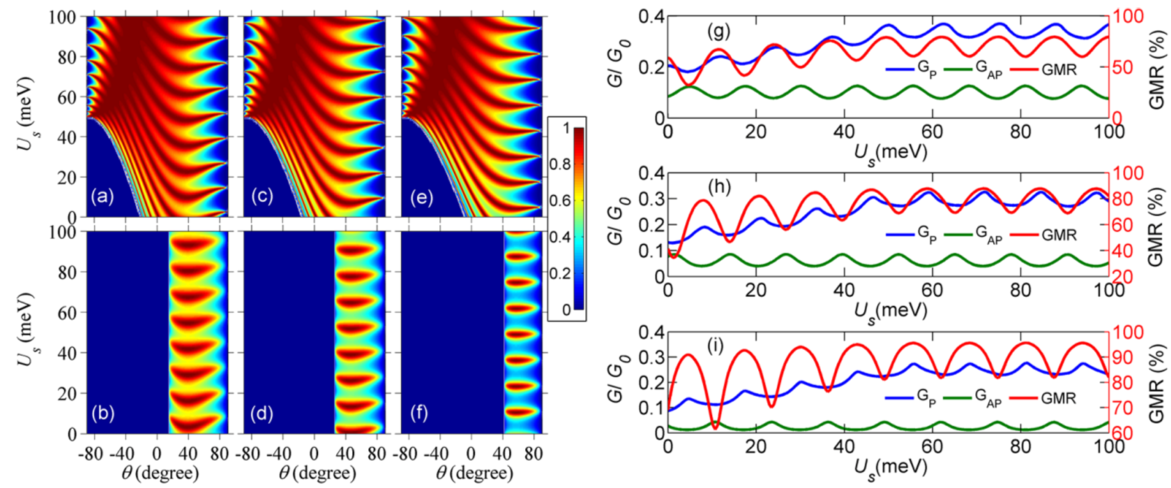

Figure 5. Contour plots of transmission probability through the FM−strained-FM−TI junction as a function of θ and U_s. E_F = 80 meV for (a) P and (b) AP configurations. E_F = 70 meV for (c) P and (d) AP configurations. E_F = 60 meV for (e) P and (f) AP configurations. Conductance G_P and G_{AP} and GMR as a function of U_s for (g) E_F = 80 meV; (h) E_F = 70 meV; and (i) E_F = 60 meV. For all cases, M_x = 50 meV, U_g = 0 meV, and d = 100 nm.

the magnetic confinements of exchange fields in the left and right regions serve as two barriers and the strain-induced negative potential in the middle region acts as a well. Therefore, this strained FM−TI junction is a natural resonant cavity and hence the Fabry-Pérot resonance should happen.

We numerically calculate the transmission probability as a function of the strain-induced potential U_s and the incident angle θ for both P and AP configurations, as demonstrated in Figure 5a−f, where we have chosen the values of E_F beyond the 100% GMR energy range. A remarkable strain-modulated Fabry-Pérot resonance occurs, but the transmission angle ranges for P and AP configurations are quite different because of the different magnetic confinements for different combinations.

However, an observation of the angle-dependent transmission resonance is challenging in experiments. We argue that GMR can be used to probe the Fabry-Pérot resonance in experiments because GMR is essentially determined by the conductance, which is related to the angular average of the transmission probability. Therefore, we further calculate the conductance and GMR as a function of the strain-induced potential for both P and AP configurations. As shown in Figure 5g−i, the conductance and GMR oscillate with the increasing strain, as a result of the Fabry-Pérot resonance. In addition, the oscillating GMR peaks and valleys are corresponding to the peaks of G_P and G_{AP}, respectively. Therefore, the oscillating GMR offers an alternative hallmark of the strain-modulated Fabry-Pérot interference for TI surface states.

4. CONCLUSIONS

In conclusion, we have investigated the strain effect on GMR in a FM−strained-FM−TI junction. The energy spectrum analysis of propagating states for this junction indicates that the spectral distribution of 100% GMR involves three types as a result of the interplay among the magnetic exchange field, the gate voltage, and the strain-induced potential. The magneto-transport calculations, including the transmission, conductance, and GMR, not only confirm the energy spectrum analysis but also predict a novel strain-controllable magnetic switch, where the applied strain with single or double cutoff values can switch between an insulating state with no GMR signal and a conducting state with 100% GMR. Beyond the energy range of the 100% GMR, the strain-modulated GMR displays a periodic oscillation and the oscillating peaks and valleys are corresponding to the Fabry-Pérot resonances for P and AP configurations. Therefore, via an experimental measurement of the strain-modulated oscillating GMR, one can probe the Fabry-Pérot quantum interference of the Dirac surface states. These strain-controllable GMR responses indicate that the proposed TI GMR straintronics is quite practical for low-power nanoscale strain sensors.

AUTHOR INFORMATION

Corresponding Authors

*E-mail: wangyh49@mail.sysu.edu.cn (Y.W.).
*E-mail: wangbiao@mail.sysu.edu.cn (B.W.).

ORCID

Yunhua Wang: 0000-0002-0436-6750

Author Contributions

‖L.L. and Y.W. contributed equally to this work.

Notes

The authors declare no competing financial interest.

ACKNOWLEDGMENTS

This work was supported financially by National Natural Science Foundation of China under Grant Nos. 11502308, 11472313, 11232015, and 11572355, Guangdong Natural Science Foundation of China under Grant No. 2016A030310205, and the fundamental research funds for the central universities under Grant No. 17lgpy31.

REFERENCES

(1) Hasan, M. Z.; Kane, C. L. Colloquium: Topological Insulators. *Rev. Mod. Phys.* **2010**, *82*, 3045.
(2) Qi, X. L.; Zhang, S. C. Topological Insulators and Superconductors. *Rev. Mod. Phys.* **2011**, *83*, 1057.
(3) Shen, S. Q. *Topological Insulators*; Springer: Berlin, 2012.
(4) Franz, M.; Molenkamp, L. *Topological Insulators, Contemporary Concepts of Condensed Matter Science*; Elsevier: New York, 2013.
(5) Bansil, A.; Lin, H.; Das, T. Colloquium: Topological Band Theory. *Rev. Mod. Phys.* **2016**, *88*, No. 021004.

(6) Zhang, H.; Liu, C. X.; Qi, X. L.; Dai, X.; Fang, Z.; Zhang, S. C. Topological Insulators in Bi_2Se_3, Bi_2Te_3 and Sb_2Te_3 with a Single Dirac Cone on the Surface. *Nat. Phys.* **2009**, *5*, 438−442.
(7) Xia, Y.; Qian, D.; Hsieh, D.; Wray, L.; Pal, A.; Lin, H.; Bansil, A.; Grauer, D.; Hor, Y. S.; Cava, R. J.; Hasan, M. Z. Observation of a Large-Gap Topological-Insulator Class with a Single Dirac Cone on the Surface. *Nat. Phys.* **2009**, *5*, 398−402.
(8) Chen, Y. L.; Analytis, J. G.; Chu, J. H.; Liu, Z. K.; Mo, S. K.; Qi, X. L.; Zhang, H. J.; Lu, D. H.; Dai, X.; Fang, Z.; Zhang, S. C.; Fisher, I. R.; Hussain, Z.; Shen, Z. X. Experimental Realization of a Three-Dimensional Topological Insulator, Bi_2Te_3. *Science* **2009**, *325*, 178−181.
(9) Hsieh, D.; Xia, Y.; Wray, L.; Qian, D.; Pal, A.; Dil, J. H.; Osterwalder, J.; Meier, F.; Bihlmayer, G.; Kane, C. L.; Hor, Y. S.; Cava, R. J.; Hasan, M. Z. Observation of Unconventional Quantum Spin Textures in Topological Insulators. *Science* **2009**, *323*, 919.
(10) Qi, X. L.; Hughes, T. L.; Zhang, S. C. Topological Field Theory of Time-Reversal Invariant Insulators. *Phys. Rev. B* **2008**, *78*, No. 195424.
(11) Qi, X. L.; Li, R.; Zang, J.; Zhang, S. C. Inducing a Magnetic Monopole with Topological Surface States. *Science* **2009**, *323*, 1184−1187.
(12) Nomura, K.; Nagaosa, N. Surface-Quantized Anomalous Hall Current and the Magnetoelectric Effect in Magnetically Disordered Topological Insulators. *Phys. Rev. Lett.* **2011**, *106*, No. 166802.
(13) Qi, X.-L.; Wu, Y. S.; Zhang, S. C. Topological Quantization of the Spin Hall Effect in Two-Dimensional Paramagnetic Semiconductors. *Phys. Rev. B* **2006**, *74*, No. 085308.
(14) Yu, R.; Zhang, W.; Zhang, H. J.; Zhang, S. C.; Dai, X.; Fang, Z. Quantized Anomalous Hall Effect in Magnetic Topological Insulators. *Science* **2010**, *329*, 61−64.
(15) Chang, C. Z.; Zhang, J.; Feng, X.; Shen, J.; Zhang, Z.; Guo, M.; Li, K.; Ou, Y.; Wei, P.; Wang, L. L.; Ji, Z. Q.; Feng, Y.; Ji, S.; Chen, X.; Jia, J.; Dai, X.; Fang, Z.; Zhang, S. C.; He, K.; Wang, Y.; Lu, L.; Ma, X. C.; Xue, Q. K. Experimental Observation of the Quantum Anomalous Hall Effect in a Magnetic Topological Insulator. *Science* **2013**, *340*, 167−170.
(16) Chen, Y. L.; Chu, J. H.; Analytis, J. G.; Liu, Z. K.; Igarashi, K.; Kuo, H. H.; Qi, X. L.; Mo, S. K.; Moore, R. G.; Lu, D. H. X.; et al. Massive Dirac Fermion on the Surface of a Magnetically Doped Topological Insulator. *Science* **2010**, *329*, 659−662.
(17) Xu, S. Y.; Neupane, M.; Liu, C.; Zhang, D.; Richardella, A.; Andrew Wray, L.; Alidoust, N.; Leandersson, M.; Balasubramanian, T.; Sánchez-Barriga, J.; Rader, O.; Landolt, G.; Slomski, B.; Hugo Dil, J.; Osterwalder, J.; Chang, T. R.; Jeng, H. T.; Lin, H.; Bansil, A.; Samarth, N.; Hasan, M. Z. Hedgehog Spin Texture and Berry's Phase Tuning in a Magnetic Topological Insulator. *Nat. Phys.* **2012**, *8*, 616−622.
(18) Wang, Y. H.; Kirtley, J. R.; Katmis, F.; Jarillo-Herrero, P.; Moodera, J. S.; Moler, K. A. Observation of Chiral Currents at the Magnetic Domain Boundary of a Topological Insulator. *Science* **2015**, *349*, 948−952.
(19) Vobornik, I.; Manju, U.; Fujii, J.; Borgatti, F.; Torelli, P.; Krizmancic, D.; Hor, Y. S.; Cava, R. J.; Panaccione, G. Magnetic Proximity Effect as a Pathway to Spintronic Applications of Topological Insulators. *Nano Lett.* **2011**, *11*, 4079−4082.
(20) Che, X.; Murata, K.; Pan, L.; He, Q. L.; Yu, G.; Shao, Q.; Yin, G.; Deng, P.; Fan, Y.; Ma, B.; Liang, X.; Zhang, B.; Han, X.; Bi, L.; Yang, Q. H.; Zhang, H.; Wang, K. L. Proximity-Induced Magnetic Order in a Transferred Topological Insulator Thin Film on a Magnetic Insulator. *ACS Nano* **2018**, *12*, 5042−5050.
(21) Burkov, A. A.; Hawthorn, D. G. Spin and Charge Transport on the Surface of a Topological Insulator. *Phys. Rev. Lett.* **2010**, *105*, No. 066802.
(22) Mondal, S.; Sen, D.; Sengupta, K.; Shankar, R. Tuning the Conductance of Dirac Fermions on the Surface of a Topological Insulator. *Phys. Rev. Lett.* **2010**, *104*, No. 046403.
(23) Wu, Z.; Peeters, F. M.; Chang, K. Electron Tunneling through Double Magnetic Barriers on the Surface of a Topological Insulator. *Phys. Rev. B* **2010**, *82*, No. 115211.
(24) Soodchomshom, B. Magneto Transport on the Surface of a Topological Insulator Spin Valve. *Phys. Lett. A* **2010**, *374*, 2894.
(25) Schwab, P.; Raimondi, R.; Gorini, C. Spin-Charge Locking and Tunneling into a Helical Metal. *Europhys. Lett.* **2011**, *93*, No. 67004.
(26) Zhang, K. H.; Wang, Z. C.; Zheng, Q. R.; Su, G. Gate-Voltage Controlled Electronic Transport through a Ferromagnet/Normal/Ferromagnet Junction on the Surface of a Topological Insulator. *Phys. Rev. B* **2012**, *86*, No. 174416.
(27) Zhang, Z.; Feng, X.; Guo, M.; Li, K.; Zhang, J.; Ou, Y.; Feng, Y.; Wang, L.; Chen, X.; He, K.; Ma, X.; Xue, Q.; Wang, Y. Electrically Tuned Magnetic Order and Magnetoresistance in a Topological Insulator. *Nat. Commun.* **2014**, *5*, No. 4915.
(28) Yokoyama, T.; Tanaka, Y.; Nagaosa, N. Anomalous Magnetoresistance of a Two-Dimensional Ferromagnet/Ferromagnet Junction on the Surface of a Topological Insulator. *Phys. Rev. B* **2010**, *81*, No. 121401.
(29) Siu, Z. B.; Jalil, M. B. A.; Tan, S. G. Magnetoresistance in Ferromagnetically Coupled Three-Dimensional Topological Insulator Strips. *IEEE Trans. Magn.* **2012**, *48*, 4250−4252.
(30) Li, X.; Duan, X.; Kim, K. W. Controlling Electron Propagation on a Topological Insulator Surface via Proximity Interactions. *Phys. Rev. B* **2014**, *89*, No. 045425.
(31) Zhang, Y.; Zhai, F. Tunneling Magnetoresistance on the Surface of a Topological Insulator with Periodic Magnetic Modulations. *Appl. Phys. Lett.* **2010**, *96*, No. 172109.
(32) Tahir, M.; Schwingenschlögl, U. Quantum Magnetotransport Properties of Topological Insulators under Strain. *Phys. Rev. B* **2012**, *86*, No. 075310.
(33) Wickles, C.; Belzig, W. Reflectionless Transport of Surface Dirac Fermions on Topological Insulators with Induced Ferromagnetic Domain Walls. *Phys. Rev. B* **2012**, *86*, No. 035151.
(34) Taguchi, K.; Yokoyama, T.; Tanaka, Y. Giant Magnetoresistance in the Junction of Two Ferromagnets on the Surface of Diffusive Topological Insulators. *Phys. Rev. B* **2014**, *89*, No. 085407.
(35) Götte, M.; Paananen, T.; Reiss, G.; Dahm, T. Tunneling Magnetoresistance Devices Based on Topological Insulators: Ferromagnet-Insulator-Topological-Insulator Junctions Employing Bi_2Se_3. *Phys. Rev. Appl.* **2014**, *2*, No. 054010.
(36) Tian, J.; Childres, I.; Cao, H.; Shen, T.; Miotkowski, I.; Chen, Y. P. Topological Insulator Based Spin Valve Devices: Evidence for Spin Polarized Transport of Spin-Momentum-Locked Topological Surface States. *Solid State Commun.* **2014**, *191*, 1−5.
(37) Scharf, B.; Matos-Abiague, A.; Han, J. E.; Hankiewicz, E. M.; Žutić, I. Tunneling Planar Hall Effect in Topological Insulators: Spin Valves and Amplifiers. *Phys. Rev. Lett.* **2016**, *117*, No. 166806.
(38) Young, S. M.; Chowdhury, S.; Walter, E. J.; Mele, E. J.; Kane, C. L.; Rappe, A. M. Theoretical Investigation of the Evolution of the Topological Phase of Bi_2Se_3 under Mechanical Strain. *Phys. Rev. B* **2011**, *84*, No. 085106.
(39) Liu, W.; Peng, X.; Tang, C.; Sun, L.; Zhang, K.; Zhong, J. Anisotropic Interactions and Strain-Induced Topological Phase Transition in Sb_2Se_3 and Bi_2Se_3. *Phys. Rev. B* **2011**, *84*, No. 245105.
(40) Bera, A.; Pal, K.; Muthu, D. V. S.; Sen, S.; Guptasarma, P.; Waghmare, U. V.; Sood, A. K. Sharp Raman Anomalies and Broken Adiabaticity at a Pressure Induced Transition from Band to Topological Insulator in Sb_2Se_3. *Phys. Rev. Lett.* **2013**, *110*, No. 107401.
(41) Li, W.; Wei, X. Y.; Zhu, J. X.; Ting, C. S.; Chen, Y. Pressure-Induced Topological Quantum Phase Transition in Sb_2Se_3. *Phys. Rev. B* **2014**, *89*, No. 035101.
(42) Feng, W.; Zhu, W.; Weitering, H. H.; Stocks, G. M.; Yao, Y.; Xiao, D. Strain Tuning of Topological Band Order in Cubic Semiconductors. *Phys. Rev. B* **2012**, *85*, No. 195114.
(43) Kim, H. S.; Kim, C. H.; Jeong, H.; Jin, H.; Yu, J. Strain-Induced Topological Insulator Phase and Effective Magnetic Interactions in Li_2IrO_3. *Phys. Rev. B* **2013**, *87*, No. 165117.

DOI: 10.1021/acsami.8b09664
ACS Appl. Mater. Interfaces 2018, 10, 28789−28795

(44) Zhang, Q.; Cheng, Y.; Schwingenschlögl, U. Series of Topological Phase Transitions in $TiTe_2$ under Strain. *Phys. Rev. B* **2013**, *88*, No. 155317.
(45) Bahramy, M. S.; Yang, B. J.; Arita, R.; Nagaosa, N. Emergence of Non-Centrosymmetric Topological Insulating Phase in BiTeI under Pressure. *Nat. Commun.* **2012**, *3*, No. 679.
(46) Xi, X.; Ma, C.; Liu, Z.; Chen, Z.; Ku, W.; Berger, H.; Martin, C.; Tanner, D. B.; Carr, G. L. Observation of a Pressure-Induced Topological Quantum Phase Transition in BiTeI. *Phys. Rev. Lett.* **2013**, *111*, No. 155701.
(47) Chen, Y.; Xi, X.; Yim, W. L.; Peng, F.; Wang, Y.; Wang, H.; Ma, Y.; Liu, G.; Sun, C.; Ma, C.; Chen, Z.; Berger, H. High-Pressure Phase Transitions and Structures of Topological Insulator BiTeI. *J. Phys. Chem. C* **2013**, *117*, 25677−25683.
(48) Agapito, L. A.; Kioussis, N.; Goddard, W. A.; Ong, N. P. Novel Family of Chiral-Based Topological Insulators: Elemental Tellurium under Strain. *Phys. Rev. Lett.* **2013**, *110*, No. 176401.
(49) Brüne, C.; Liu, C. X.; Novik, E. G.; Hankiewicz, E. M.; Buhmann, H.; Chen, Y. L.; Qi, X. L.; Shen, Z. X.; Zhang, S. C.; Molenkamp, L. W. Quantum Hall Effect from the Topological Surface States of Strained Bulk HgTe. *Phys. Rev. Lett.* **2011**, *106*, No. 126803.
(50) Winterfeld, L.; Agapito, L. A.; Li, J.; Kioussis, N.; Blaha, P.; Chen, Y. P. Strain-Induced Topological Insulator Phase Transition in HgSe. *Phys. Rev. B* **2013**, *87*, No. 075143.
(51) Sklyadneva, I. Y.; Rusinov, I. P.; Heid, R.; Bohnen, K. P.; Echenique, P. M.; Chulkov, E. V. Pressure-Induced Topological Phases of KNa_2Bi. *Sci. Rep.* **2016**, *6*, No. 24137.
(52) Sun, Y.; Wang, Q. Z.; Wu, S. C.; Felser, C.; Liu, C. X.; Yan, B. Pressure-Induced Topological Insulator in NaBaBi with Right-Handed Surface Spin Texture. *Phys. Rev. B* **2016**, *93*, No. 205303.
(53) Shao, D.; Ruan, J.; Wu, J.; Chen, T.; Guo, Z.; Zhang, H.; Sun, J.; Sheng, L.; Xing, D. Strain-Induced Quantum Topological Phase Transition in Na_3Bi. *Phys. Rev. B* **2017**, *96*, No. 075112.
(54) Peng, H.; Dang, W.; Cao, J.; Chen, Y.; Wu, D.; Zheng, W.; Li, H.; Shen, Z. X.; Liu, Z. Topological Insulator Nanostructures for Near-Infrared Transparent Flexible Electrodes. *Nat. Chem.* **2012**, *4*, 281−286.
(55) Zhao, L.; Liu, J. W.; Tang, P. Z.; Duan, W. H. Design of Strain-Engineered Quantum Tunneling Devices for Topological Surface States. *Appl. Phys. Lett.* **2012**, *100*, No. 131602.
(56) Liu, Y.; Li, Y. Y.; Rajput, S.; Gilks, D.; Lari, L.; Galindo, P. L.; Weinert, M.; Lazarov, V. K.; Li, L. Tuning Dirac States by Strain in the Topological Insulator Bi_2Se_3. *Nat. Phys.* **2014**, *10*, 294.
(57) Park, S. H.; Chae, J.; Jeong, K. S.; Kim, T. H.; Choi, H.; Cho, M. H.; Hwang, I.; Bae, M. H.; Kang, C. Reversible Fermi Level Tuning of a Sb_2Te_3 Topological Insulator by Structural Deformation. *Nano Lett.* **2015**, *15*, 3820−3826.
(58) Korkusinski, M.; Hawrylak, P. Quantum Strain Sensor with a Topological Insulator HgTe Quantum Dot. *Sci. Rep.* **2014**, *4*, No. 4903.
(59) Tang, E.; Fu, L. Strain-Induced Partially Flat Band, Helical Snake States and Interface Superconductivity in Topological Crystalline Insulators. *Nat. Phys.* **2014**, *10*, 964−969.
(60) Zeljkovic, I.; Walkup, D.; Assaf, B. A.; Scipioni, K. L.; Sankar, R.; Chou, F.; Madhavan, V. Strain Engineering Dirac Surface States in Heteroepitaxial Topological Crystalline Insulator Thin Films. *Nat. Nanotechnol.* **2015**, *10*, 849−853.
(61) Yokoyama, T. Spin and Valley Transports in Junctions of Dirac Fermions. *New J. Phys.* **2014**, *16*, No. 085005.
(62) Drüppel, M.; Krüger, P.; Rohlfing, M. Strain Tuning of Dirac States at the SnTe (001) Surface. *Phys. Rev. B* **2014**, *90*, No. 155312.
(63) Zhao, L.; Wang, J.; Gu, B. L.; Duan, W. Tuning Surface Dirac Valleys by Strain in Topological Crystalline Insulators. *Phys. Rev. B* **2015**, *91*, No. 195320.
(64) Seo, J.; Roushan, P.; Beidenkopf, H.; Hor, Y. S.; Cava, R. J.; Yazdani, A. Transmission of Topological Surface States through Surface Barriers. *Nature* **2010**, *466*, 343−346.
(65) Wang, J.; Li, W.; Cheng, P.; Song, C.; Zhang, T.; Deng, P.; Chen, X.; Ma, X.; He, K.; Jia, J.; Xue, Q. K.; Zhu, B. F. Power-Law Decay of Standing Waves on the Surface of Topological Insulators. *Phys. Rev. B* **2011**, *84*, No. 235447.
(66) Dolcini, F. Full Electrical Control of Charge and Spin Conductance through Interferometry of Edge States in Topological Insulators. *Phys. Rev. B* **2011**, *83*, No. 165304.
(67) An, J.; Ting, C. S. Surface States Scattering from a Step Defect in the Topological Insulator Bi_2Te_3. *Phys. Rev. B* **2012**, *86*, No. 165313.
(68) Fu, Z. G.; Zhang, P.; Chen, M.; Wang, Z.; Zheng, F. W.; Lin, H. Q. Anisotropic Fabry-Pérot Resonant States Confined within Nano-Steps on the Topological Insulator Surface. *Sci. Rep.* **2014**, *4*, No. 5544.
(69) Hong, S. S.; Zhang, Y.; Cha, J. J.; Qi, X. L.; Cui, Y. One-Dimensional Helical Transport in Topological Insulator Nanowire Interferometers. *Nano Lett.* **2014**, *14*, 2815−2821.

DOI: 10.1021/acsami.8b09664
ACS Appl. Mater. Interfaces 2018, 10, 28789−28795